University of Szeged
Department of Image Processing and Computer Graphics

A Pixel-based Discrete Tomographic Technique and Its Applications

Summary of the Ph.D. thesis

by

Zoltán Kiss

Thesis advisor

Attila Kuba, Ph.D.

University of Szeged
Ph.D. School in Computer Science

Szeged
2011

1   Introduction

In physics and image processing, a common problem is how to obtain information about the interior of an object in a non-destructive manner (non-destructive testing, NDT); that is, without damaging it in any way. For this purpose, several kinds of physical methods have been developed like X-ray, gamma-ray and neutron imaging. In industrial metallic material examinations, neutron and gamma-ray sources are generally used, while X-ray sources are often applied for non-metallic objects. The imaging tool for reconstructing objects from their projection images, obtained from some radiation source, is called *tomography*.

In practice, the acquisition of such projections can be a costly and time consuming procedure, so one of the main efforts is to minimize the number of projections used for the reconstruction. One way of doing this is by restricting the type of objects for reconstruction, and applying a customized tomographic method that exploits some a priori knowledge to compensate for having a reduced number of projections.

Discrete tomography (DT) is a special field of tomography where the object to be reconstructed consists of a small number of homogeneous materials/regions that can be characterized by *finitely many known absorption values*. It means that, using DT, only a special class of objects can be reconstructed. Accordingly, the result of a DT reconstruction is a *discrete image* having values only corresponding to the known absorption coefficients. Moreover, in many cases some *a priori information* is also available about the object under investigation. For example, its structure is similar to a template object, or the object is made of materials that are nearly homogeneous. Since industrial objects are usually made of just a few materials, DT plays an important role in industrial NDT, where the internal configuration of a specimen needs to be determined.

In DT one cleverly uses the information that the function has a known discrete range. This is the main difference between the DT and classical computed tomography, as in the latter case the function/object can in general have arbitrary (non-negative) values. A knowledge of discrete absorption values can allow one, using DT methods, to reconstruct objects like these from a small number of projections (e.g. 4–10) and/or to improve the quality of the reconstruction.

In the thesis a new DT method is presented that reconstructs objects from their *parallel* projections. The method treats the object being investigated as a digital image, and the reconstruction problem is an optimization task that is solved by simulated annealing.

2   The pixel-based reconstruction method

The new pixel-based method (published by the author in [5, 9]) essentially frames the reconstruction problem as an optimization task, and minimizes the objective functional

$$\Phi(f) = \sum_{\vartheta} \| \left[\mathcal{R}f \right](\vartheta) - P_\vartheta \|^2 + \gamma \, \phi(f) \,, \tag{1}$$

where P_ϑ denotes the ϑ projection, f is the 2-dimensional image function that approximates the solution, $\left[\mathcal{R}f \right](\vartheta)$ denotes the projection of image f calculated at angle ϑ, $\|.\|$ is the Euclidean norm, $\phi(f)$ is the so-called *regularization (or penalty) term*, and $\gamma \geq 0$ is the *regularization parameter*.

In Eq. 1 the first term is a functional, which represents the distance between the projections of f and the given projection data P_ϑ. This term tells us how well the projections of f

approximate the given projections. As mentioned above, the fewer the number of projections used, the more *a priori information* should be exploited. Some pieces of information can be incorporated into the regularization term, which help one choose the right solution from the number of possible reconstructions.

A key question is, of course, what optimization method should be chosen for the minimization of $\Phi(f)$ defined in Eq. 1. Since we usually have no information about the properties of the objective functional, and there is no technique available that tells us how to find a good initial point that is close to a global minimum, the method used must be chosen from the family of discrete global optimizers. Here the author opted for simulated annealing.

2.1   The reconstruction strategy

The reconstruction method was mainly based on the article [16], and was developed in the following way.

2.1.1   Iterative core

A reconstruction result is obtained via a sequence of approximating image functions $f^{(0)}, f^{(1)}, \ldots$ such that $|\Phi(f^{(i)}) - \Phi(f^\star)| \to 0$ when $i \to \infty$, where $f^{(i)}$ denotes the image function in the ith iteration, $i \in \mathbb{Z}^{0,+}$, and $f^\star$ is a minimum locus of Φ. For each iteration step, the $(i+1)$th image function is constructed by perturbing the ith image according to a predefined *modification rule*.

2.1.2   Perturbation of $f^{(i)}$

The simplest example for the modification process is when the range of the function $f^{(i)}$ consists of two values only, such as 0 and 1. The rule for changing the binary image function $f^{(i)}$ is quite simple. Let us randomly choose a pixel of $f^{(i)}$, and switch its (0 or 1) intensity to the other intensity value. In this way we get the new image f', differing from $f^{(i)}$ by one pixel only.

Figure 1: A 3-level discrete image.

When $f^{(i)}$ contains more than two values, $f^{(i)}$ is a so-called *multi-level image function* (see Figure 1). A multi-level image takes its values from a known $D = \{k_1, k_2, \ldots, k_n\}$ discrete set of intensity values, where $n\,(\geq 3)$ is an integer, namely the cardinality of the range of

$f^{(i)}$. Hence the modification rule also differs from the one used for binary images. If $f^{(i)}$ has the value k_j $(1 \leq j \leq n)$ at the randomly selected position, then set its new value to k_l in f', where l is randomly picked from the discrete set $\{1, \ldots, n\}$. An alternative modification strategy might be when k_l is calculated according to the following formula:

$$k_l = \begin{cases} k_{j-1}, & \text{if } 2 \leq j \leq n-1 \text{ and } \xi < 0.5 \\ k_{j+1}, & \text{if } 2 \leq j \leq n-1 \text{ and } \xi \geq 0.5 \\ k_{j-1}, & \text{if } j = n \\ k_{j+1}, & \text{if } j = 1 \end{cases}, \tag{2}$$

where ξ is a probability variable of the uniform distribution taking its value from $[0, 1)$.

2.1.3 Acceptance criterion

An f' perturbation of $f^{(i)}$ is accepted if $\Phi(f') \leq \Phi(f^{(i)})$. After, let $f^{(i+1)} = f'$; that is, the optimization procedure carries on with the newly created f' image in the next iteration. Otherwise, if $\Phi(f') > \Phi(f^{(i)})$, f' can still be accepted with a certain probability depending on $\Delta\Phi = \Phi(f') - \Phi(f^{(i)})$, the current temperature, and a randomly generated z value of the uniform distribution from the interval $(0, 1)$, allowing the optimizer to escape from local minima. The acceptance condition for bad configurations is given by the Metropolis criterion, namely

$$e^{-\Delta\Phi/\kappa T^{(i)}} > z, \tag{3}$$

where κ is the Boltzmann constant ($11.3805 \times 10^{-23} m^2 kg\, s^{-2} K^{-1}$) and $T^{(i)}$ is the temperature in the current iteration. The denominator in the exponent is the product of κ and $T^{(i)}$, reflecting the fact that the individual values here are irrelevant from an algorithm point of view. It allows us to fix $\kappa = 1$, instead of using the original miniscule value of Boltzmann constant, thus avoiding the need for having extremely high temperatures to get reasonable $\kappa T^{(i)}$ products.

2.1.4 Temperature scheduling

$T^{(i)}$ decreases during the iterations according to a suitable *schedule*, but the temperature is not reduced for each iteration, only in the case where the optimizer attains an equilibrium state at the current temperature level. By equilibrium we mean that the optimizer is unable to reduce the objective values any further due to the many accepted bad configurations at a given $T^{(i)}$ level. This variant of SA is called *homogeneous simulated annealing*.

A pitfall of the technique is how 'equilibrium' should be defined mathematically. For this purpose, an easily computable indicator was chosen, which is based on the variance of the last Φs. Formally, the method attains equilibrium if

$$\sigma_1^2 < \sigma_0^2, \tag{4}$$

where σ_t^2 is the variance calculated from $\Phi_{i-tv}, \Phi_{i-tv-1}, \ldots, \Phi_{i-(t+1)v+1}$, $\Phi_i = \Phi(f^{(i)})$, and v denotes the sample size the variance is calculated from. That is, a session terminates at a given temperature level if the variance of Φs is greater in the last v than in the preceding v iterations.

Another interesting question is how the temperature should be reduced every time the equilibrium state is attained. For this,

$$T^{(i+1)} = T^{(i)} \cdot h \tag{5}$$

is generally used, where h is called the *cooling factor*, taking its value from the interval $(0, 1)$. In other words, $T^{(i)}$ is decreased by $(1 - h) \cdot 100\%$ each time $T^{(i)}$ is reduced.

2.1.5 Termination condition

Since the optimization process could run endlessly, a termination criterion has to be included in the algorithm. The most obvious termination condition is when some f configuration is found where the first term of $\Phi(f)$ attains 0. However, especially under noisy circumstances, the projections are usually inconsistent, and no such f satisfying the projections exists. Such situations have been extensively analyzed in [6]. A better solution is when an *efficiency measure* is computed, which indicates that no further improvements can be perceived in the recent objective values. It is defined by the ratio

$$\frac{N_{rej}}{N_{att}} . \tag{6}$$

Here N_{rej} denotes the number of rejected configurations in the last N_{att} iterations.

3 Simulations

In order to test the pixel-based reconstruction on software phantoms, a simulation system was implemented that was designed to generate parallel projections of arbitrary grey-level images, to corrupt the projections by additive Gaussian noise, and to evaluate the goodness of reconstructions.

It was necessary to examine the behaviour of the DT technique when the input parameters are adjusted within reasonable ranges. Becoming familiar with the nature of the parameters gives vital information on how to fine-tune the reconstruction when a poor result is obtained.

As the reconstruction method is a statistical one, its robustness and efficiency cannot be judged from a single reconstruction. Accordingly, each parameter set-up was executed 50 times, so the author's simulation experience was based on average reconstruction results. It led to a remarkable amount of statistical data. For example, over 170 parameter configurations were examined just for the two-valued images, which meant that over 8500 binary reconstructions were performed.

The author published his results in [5, 9, 10].

3.1 Measuring the reconstruction quality

The goodness of the reconstruction was measured by the *relative mean error* (RME). Let f^o and f^r be two discrete functions over a $h \times h$ lattice set, where f^o has at least one non-zero element. The RME for binary images is defined by the formula

$$\mathrm{RME}\left(f^o, f^r\right) = \frac{\sum\limits_i |f_i^o - f_i^r|}{\sum\limits_i f_i^o} \cdot 100\% , \tag{7}$$

and by

$$\mathrm{RME}^{\mathrm{m}}\left(f^{\mathrm{o}}, f^{\mathrm{r}}\right) = \frac{\sum\limits_{i} |f_i^{\mathrm{o}} - f_i^{\mathrm{r}}|}{\sum\limits_{i} \lceil f_i^{\mathrm{o}} \rceil} \cdot 100\% \tag{8}$$

for multi-level ones, where $i = 1, \ldots, h^2$, and $f_i^{\mathrm{o}}, f_i^{\mathrm{r}} \in \{0, 1\}$ denote the value of the ith pixel in the original and reconstructed image, respectively. Here $\lceil . \rceil$ denotes the ceiling function, and it is used to compute the number of non-zero pixels in the original image.

It is obvious that $\mathrm{RME} \geq 0$, and $\mathrm{RME} = 0$ holds if and only if $f_i^{\mathrm{o}} = f_i^{\mathrm{r}}$. It is also clear that a smaller value of RME indicates a better reconstruction result, and RME can exceed 100%. The latter can be deduced directly from the formula when there are more misplaced pixels in f^{r} than the number of non-zero ones in f^{o}.

3.2 Binary results

For the binary tests two phantoms (Figure 2) were created, where the circular image could be regarded as nearly the worst-case binary object. Using these objects the author investigated the effect of changing the initial temperature, the cooling factor, the termination criterion, the amount of noise added to the projections, and the number of projections used for the reconstruction. The author also wanted to know whether the method was sensitive to the geometrical properties of the phantom.

(a) Binary phantom image containing circle-shaped objects.

(b) Binary phantom image containing square-shaped objects.

Figure 2: Binary phantom images used in the simulation tests.

The simulation tests revealed that, from a goodness of reconstruction point of view, the crucial parameter is the cooling factor. That is, an improper choice of its value can lead to a reconstruction of bad quality or entail the premature termination of the reconstruction process. In another simulation experiment the author observed that if the initial temperature is high, the method runs only a bit longer than choosing a more reasonable lower value. However, when $T^{(0)}$ is too low, the optimizer can get stuck in a local minimum and yield a bad result.

The sensitivity to the geometrical properties of the object to be reconstructed could also be demonstrated. The conclusion could be drawn that an object having edges parallel to the beams results in sharp gaps in the objective (cf. the natural projections of Figure 2(b)), and

this can be readily discovered by the optimizer, even in the case of a suboptimal parameter set-up. In other words, when the phantom image comprises shapes with smooth projections, the optimizer has an uphill task due to the probably larger number of shallow local minima.

Next, as the method is a stochastic one, it was also an important result that the pixel-based technique can provide a perfect reconstruction when a sufficient number of projections is used.

3.3 Reduction of the noise effects

Since, especially in the case of industrial objects, it may often be assumed that the cross-section to be reconstructed contains contiguous regions of the same intensity, the smoothness property was the most obvious a priori to be exploited. The regularized reconstructions from noisy projections [9] were carried out using the following mathematical description of smoothness:

$$\phi(f) = \sum_{x,y} \sum_{u,v} \left(f\left(x,y\right) - f\left(x-u, y-v\right) \right) \cdot \exp\left[-\frac{(u-\mu_x)^2}{2\sigma_x^2} - \frac{(v-\mu_y)^2}{2\sigma_y^2} \right]. \tag{9}$$

This function penalizes the resultant images containing non-homogeneous regions, and prefers image functions that consist of large contiguous ones. In other words, Eq. 9 computes a bigger ϕ value for noisy/detail-rich image parts and a smaller one for smooth/homogeneous regions.

Figure 3 readily shows how the regularization term diminished the noise effect in the reconstructions, but it should be mentioned that a bigger γ is inclined to join adjacent objects that are distinct in the average reconstructions. Nevertheless, it is quite apparent that the technique provides improved results with the assumption of smoothness, whose property can also be exploited for the reconstruction of physically measured projections.
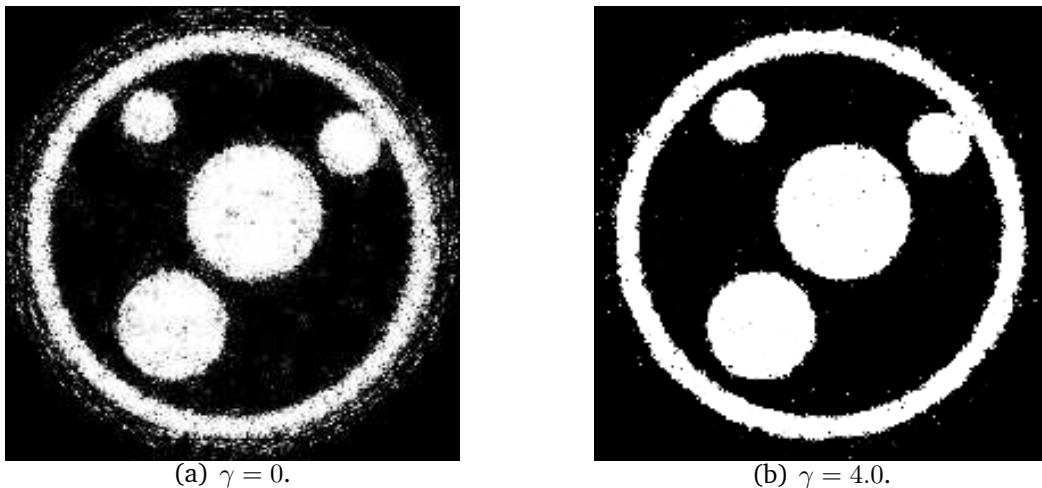

(a) $\gamma = 0$.   (b) $\gamma = 4.0$.

Figure 3: Non-regularized and regularized average reconstruction results using 16 noisy ($\sigma = 10.0$) projections.

3.4 Multi-level reconstruction

For the 3-level extension, the first perturbation strategy described in Section 2.1 was applied, where the modification rule was the random choice of a value from the set of possible intensity

levels. In this way, the fully stochastic nature of the technique could be retained. The second strategy, where the intensity levels were always replaced with the neighbouring intensity values, quite often got stuck in local minima and usually underperformed the fully stochastic version in comparative tests.

The images in Figure 4(a) indicate that the multi-level reconstructions produced similar results to the noisy images, which was probably caused by the increased number of switching components [7] in the case of an higher number of intensity levels. The results could be easily rectified by turning on the regularization term, as shown in Figure 4(b). However, it meant that the borders were sometimes replaced by an intermediary intensity of neighbouring regions.
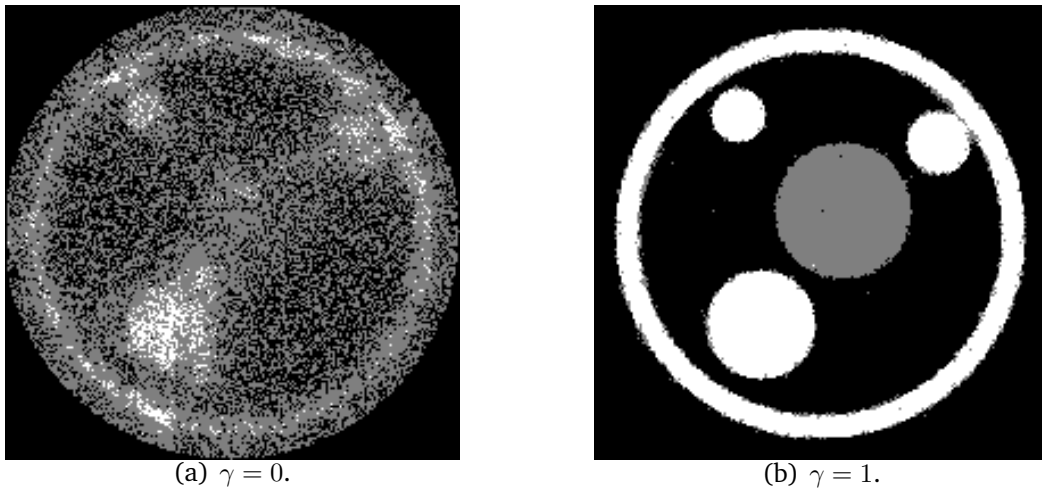

(a) $\gamma = 0$. (b) $\gamma = 1$.

Figure 4: Two noiseless reconstructions of the 3-level phantom image. (12 projections, 400 measurements/projection.)

4 Pre-processing

Physically measured projections are usually unsuitable for an immediate reconstruction due to the effects the images are distorted by and the transformation needed to get line integrals instead of the number of impacting particles. As these distortions can cause serious degradations in the reconstruction results, it is necessary to correct them as best one can. Hence a feasible sequence of correction steps was developed.

The pre-processing results were published in [1, 12].

4.1 The acquired projection

In non-destructive testing (NDT) the objects are imaged by rays coming from an external radiation source. The rays passing through the object are then partially absorbed, while the unabsorbed particles strike the detector bins. The numbers of impacting particles (counted by the detector bins) give the intensity values in the projection images.

The connection between the initial and transmitted (unabsorbed) intensities, I_S and I_D, respectively, can be expressed as a function that depends on the absorption (or attenuation) coefficient μ of the object. Namely,

$$I_D = I_D(s, \vartheta) = I_S \cdot e^{-\int_S^D \mu(u)du}, \tag{10}$$

where S and D denote the source and the detector. This equation is a basic relation in *transmission tomography*, and it is also known as Beer's law. (See Figure 5.)
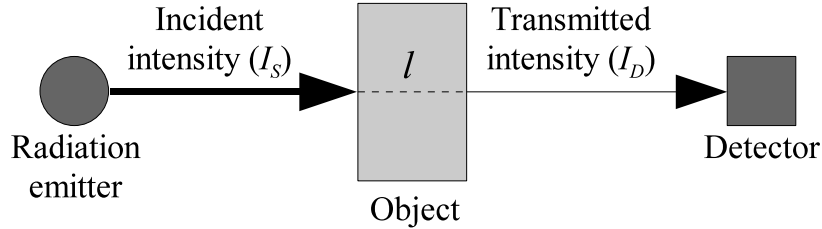

Figure 5: Scheme used to illustrate Beer's law and the phenomenon of radiation attenuation. I_S is the intensity emitted by the radiation source, I_D is the intensity measured by the detector, and l is the length of the line segment intersected by the projection beam and the homogeneous object.

In practice, the task is to determine μ by making the assumption that I_S and I_D are measurable. The value of μ is immediately implied by the logarithmic transformation of Eq. 10, and it has the form

$$\int_S^D \mu(u)du = \ln(I_S/I_D). \tag{11}$$

Several inferences can be drawn from this equation. The left hand side of the equation is zero if and only if $I_S = I_D$, meaning that there is no attenuation when the beam is being transmitted. When the detected intensity is zero ($I_D = 0$), then no attenuation can be determined, since the fraction on the right hand side cannot be interpreted. The best that can be done is to assume an infinitely large absorption under such circumstances. In real circumstances, the zero measurements are usually caused by an overly short exposure time, which can be eliminated by choosing longer acquisition periods for the projections.

4.2   The pre-processing steps

As mentioned previously, the measurements are usually imperfect and corrupted by a number of effects. These effects can be attributed to the physical properties of the imaging system and can cause serious degradation in the reconstruction results. The following pre-processing steps were devised for the problems encountered by the author during his study.

1. *Cropping.* The projection of the object being investigated often covers just a small part of the whole acquired image, so the relevant part is selected and cropped from all projections. These cropped projection images of a smaller size are used in the later pre-processing steps and reconstruction. The reconstruction from cropped projections requires less memory and computational time; in addition, the smaller (probably distorted) the background area involved in the reconstruction, the better the reconstruction quality can be expected.

2. *Motion correction.* It can also happen that the settings of the projection images were not perfect and that some of the images were not taken from the right position. A consequence might be that the images are the rotated or translated versions of the correct ones. This is why two new pre-processing methods were employed in the system.

   (a) The first method is suitable when opposite projections are available, and the positioning errors can be modelled such that the projections of the rotation axis are translated horizontally in the projection images (along a sine curve, say). In this case the necessary transformation is the horizontal translation of each projection image, whose parameters can be determined by overlapping the flipped image and its opposite version ('centre of rotation correction' [12]).

   (b) The second method presumes that the projections of the object are very similar (e.g. the projections of a tube from the directions perpendicular to the tube's axis). By applying a suitable rigid registration on all the projections to a selected reference image, one can find the correct projection settings. The registration technique applied here was Tanacs's *rigid* method published in [17].

3. *Homogeneity correction.* Sometimes the detector plane is not uniformly sensitive in the whole field of view. This problem can be lessened if an '*empty*' image is available. The empty image is acquired by imaging a homogeneous radiation flux. If the detector system is uniformly sensitive, then this image is almost constant. Otherwise, the empty image reveals how much correction (multiplication) is necessary, pixel by pixel in each projection, in order to obtain more constant images. The correction can be described mathematically in the following way. For each pixel i of all P_ϑ projections,

$$r_{\vartheta,i} = p_{\vartheta,i} \cdot \frac{1}{p_{empty,i}}\,, \tag{12}$$

where $p_{\vartheta,i}$, $p_{empty,i}$, and $r_{\vartheta,i}$ denote the intensity of the ith pixel in the original ϑ projection (P_ϑ), in the empty image (P_{empty}), and in the corrected ϑ projection (R_ϑ), respectively.

4. *Intensity correction.* It might happen that the total intensities of the projection images vary during the acquisition period. The reason could be variations in the neutron flux or the electronic properties of the camera, as described in Section 4.1. When this occurs each pixel j in each image P_{ϑ_i} ($i = 1, \ldots, m$) should be multiplied by a suitable positive real constant C_i such that

$$C_i \sum_{j=1}^{d} p_{\vartheta_i,j} \approx K\,, \tag{13}$$

where d is the number of pixels in a projection, and K is a positive real denoting the desired total intensity. In other words, the total intensity values will be roughly the same in the corrected projections. For instance, for an arbitrary fixed $\tilde{i} \in \{1, \ldots, m\}$ reference projection, K can be calculated as

$$K = \sum_{j=1}^{d} p_{\vartheta_{\tilde{i}},j} \tag{14}$$

and C_i can be defined by

$$C_i = \frac{K}{\sum_{j=1}^{d} p_{\vartheta_i,j}} \qquad (15)$$

for all $i = 1, \ldots, m$. The author applied this form of intensity correction in the experiments.

After this step the flickering phenomenon, which is often visible when playing the projection sequence like a movie, diminishes.

5. *Isolated specks.* The tomographic projections often contain white pixels, which appear as isolated points having a very different intensity value compared with its neighbourhood, and can give rise to strong white lines in the reconstructions. In order to eliminate this kind of problem in the projections, we performed thresholded median filtering. For each pixel i of each P_ϑ projection

$$r_{\vartheta,i} = \begin{cases} p_{\vartheta,i} & \text{if } |p_{\vartheta,i} - \text{med}(\text{NRH}(P_\vartheta, i, n))| \leq \text{ thr}, \\ \text{med}(\text{NRH}(P_\vartheta, i, n)) & \text{otherwise}, \end{cases}$$

where $r_{\vartheta,i}$ is the intensity of the ith pixel in the corrected image R_ϑ, $\text{med}(.)$ is the median operator, thr is a suitable threshold constant, and $\text{NRH}(P_\vartheta, i, n)$ is a set which contains the intensity values of the n-neighbourhood pixels of i in the image P_ϑ.

6. *Logarithmic transformation.* In order to get the approximate values of the line integrals (i.e. instead of working with the number of impacting particles counted by the detectors), a logarithmic transformation needs to be performed on the measured intensity values, as given in Eq. 11. This transformation is always performed on the input data.

5 Reconstructions of physical phantoms

The author tested the pixel-based technique on three physical phantoms [10, 12], where the projections were acquired by applying X-ray, neutron and gamma radiation sources. For each test he used so-called *reference cylinders* with the geometry depicted in Figure 6, which were composed of different materials depending on the type of radiation applied. All the cylinders contained three bores of various diameters and depths in an asymmetric arrangement, and were filled up with different materials. That is, the projection beams transmitted at least three materials; namely air, the material the cylinder was composed of, and the materials the bores were filled up with.

5.1 Determination of intensity levels

The next problem was that the exact intensity levels of the image to be reconstructed were unknown. Under ideal monochromatic (single-energy radiation) circumstances, the intensity values could be calculated from the linear attenuation coefficients given in the literature. However, the production of monochromatic beams requires expensive and complicated devices, hence they are usually not employed in real experiments. That is, the absorption coefficients calculated in any way, can be viewed as approximate values only. This fact violated one of the basic DT assumptions, namely that the exact attenuation coefficients of the few
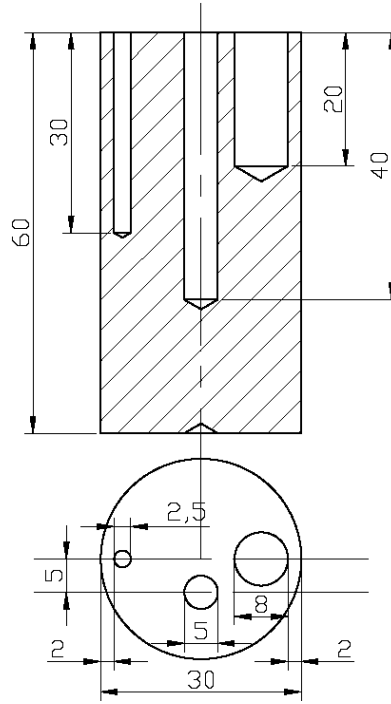
Figure 6: Diagram of the physical phantom object used in the experiments.

materials comprising the object should be known in advance. So a technique had to be found to estimate the correct absorption values.

In order to determine the intensity values, the idea [5] was to approach the discrete image f (recall that f denotes the 3-level image sought) with the reconstruction of another image $\tilde{f}$ having more intensity values than f, while the smoothness term is kept turned on in the objective. An approximation of the intensities can be obtained by determining the local maxima in the histogram of $\tilde{f}$. Since it may be assumed that the intensities have a Gaussian distribution around the original levels, the approximation can be more exact if the values are determined by fitting a sum of the appropriate number (currently three) of Gaussian functions to the histogram. The mean values of these Gaussians can be regarded as approximations of the original values in this case.

5.2 Reconstruction of reference cylinders

After executing the necessary pre-processing steps and determining the discrete set of intensity levels, the three cylinders were reconstructed from a small number of projections by the pixel-based DT technique (Figure 7), FBP and ART. Generally speaking, the classical cross-sections became very streaky due to the non-ideal conditions for a continuous reconstruction. It was also found that the DT technique reflects the real absorption values more realistically than those for FBP and ART because it does not (cannot) show false intensity levels. Instead it breaks up the larger homogeneous regions into smaller ones, and a certain level of inhomogeneity can be assumed in such cases. It should also be mentioned that the DT technique did not give better results than the classical ones, when sufficient number of projections were available. However, when the reconstruction was performed with just a small number of projections, the pixel-based technique unquestionably outperformed FBP and ART.
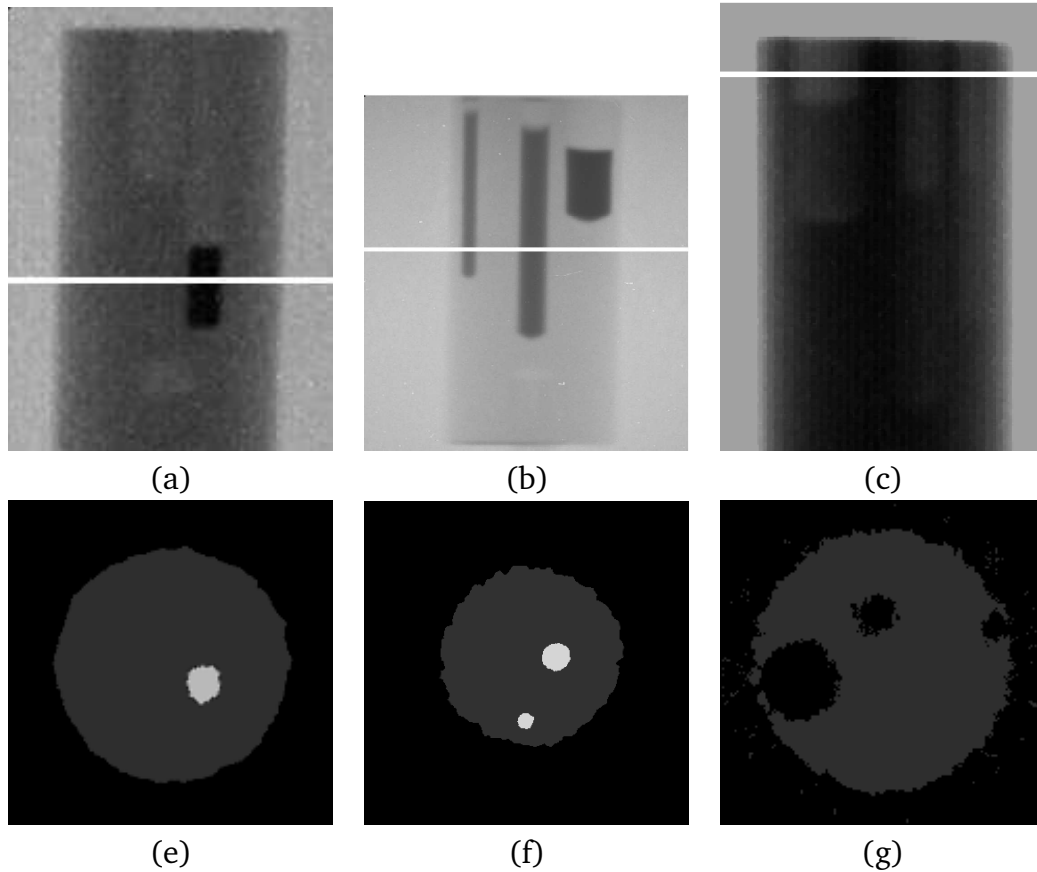
Figure 7: (a) A projection of a Plexiglas cylinder taken using an X-ray source. (b) A projection of an aluminum cylinder taken using a neutron source. (c) A projection of an iron cylinder taken using a gamma-ray source. (d) Pixel-based reconstruction of the cross-section marked in (a) using 9 projections. (e) Pixel-based reconstruction of the cross-section marked in (b) using 10 projections. (f) Pixel-based reconstruction of the cross-section marked in (c) using 9 projections.

6   Reconstructions of physical objects

One interesting question was how the method would perform when the discrete set of intensity levels could not be determined. It may happen when the object contains inhomogeneous materials, for instance. In this case an enhanced set of intensity levels must be applied for the reconstruction, which can be achieved by the proper equidistant discretization of the full range of possible intensity levels, as was done in the determination of the intensity levels. In this way, the reconstructed cross-section cannot really be regarded as a discrete image or a continuous one, but it may lie somewhere between the two. Using this technique a cardiac pacemaker battery and a boron-carbide control rod were successfully reconstructed.

The author published his results in [3, 9].

6.1   Reconstruction of a cardiac pacemaker battery

The author was contacted by physicists from the Hahn-Meitner Institute, who wanted to know whether the DT method was capable of reconstructing the battery of a pacemaker using just a small number of projections [9]. The battery was composed of two main components; namely the intrinsic part containing the electrically charged material, and its housing. It was a topic

of interest because there is a strong connection between its lifetime and the distribution of the charged material, hence the physicists wanted to have a spatial model so as to inspect the intrinsic part.

There were 200 neutron projections[1] acquired equiangularly with a spacing of 0.9°, where each projection had a size of 447×512. Although the number of projections was large, it was intended to be reduced in the subsequent examinations of other pacemaker batteries.

After the reconstruction of 50 slices, the cross-sections were turned into a 3-dimensional volume-rendered model. In spite of the severe conditions, the irregular distribution of charged material is quite visible in each DT reconstruction (using 20 projections) in Figure 8(a), and even clearer with multiple cross-sections in the volume-rendered spatial model in Figure 8(b). While the reconstructions produced by the classical methods using the same number of projections could not result in a 3-dimensional model of the same quality.
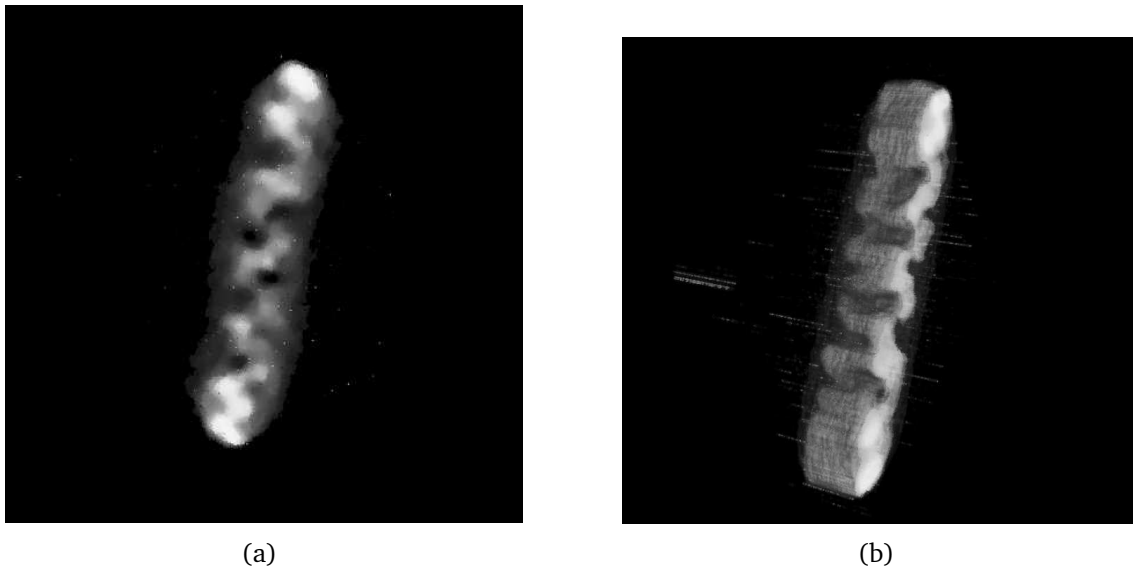

(a)   (b)

Figure 8: (a) Pixel-based reconstruction of a cross-section. (b) Volume-rendered view of the cardiac pacemaker battery got from 50 slices. The reconstructions were performed using 20 projections.

6.2 Reconstruction of a boron-carbide control rod

Another live test [3] was performed on the projections of a control rod. Control rods are usually made of a tube filled with a neutron absorber, where the absorber is a chemical element with a high neutron absorption capability used to moderate the particle flux within the reactor core. However, any undesirable changes in the distribution of the absorber adversely affects its effectiveness, so it was a vital examination from a nuclear reactor safety point of view.

There were 18 neutron images[2] taken from a single control rod having an aluminum wall (1 mm thickness) and containing a boron absorber. The goal of the examinations was to find evidence and visualize the irregular absorber distribution, especially at the bottom of the rod, where even the presence of bubble-like helium accumulations were supposed (Figure 9).

---

[1]The projections were provided by Prof. Wolfgang Treimer (Hahn-Meitner Institute, Berlin).

[2]The projections were provided by Prof. Márton Balaskó (Hungarian Academy of Sciences KFKI Atomic Energy Research Institute, Budapest).
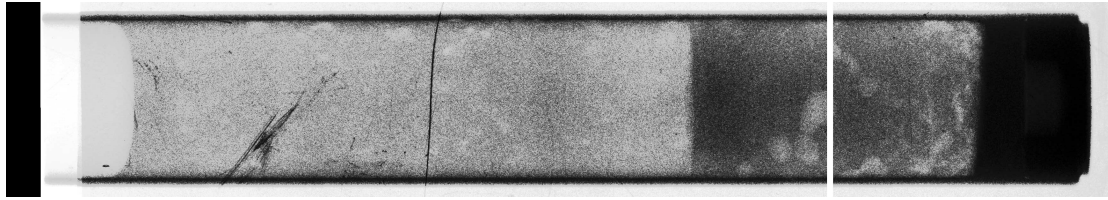
Figure 9: 10° and 70° projections of the control rod after a rigid registration and brightness, contrast, gamma adjustment. The images have been rotated by 90° counterclockwise. The darker lower section is boron-carbide with supposed helium inclusions.

Although is was assumed that the distribution of the absorber material was inhomogeneous, the control rod was also reconstructed as a 3-level object from 9 projections. The application of the pixel-based technique under such circumstances means one expects the bad reconstruction of the absorber part, which was confirmed by the 3-dimensional model of the reconstructed slices in Figure 10(a). It is quite apparent that the DT technique still performed well at the bottom of the rod (right hand side of the figure) where no absorber was present in the cross-sections, but they became seriously corrupted as soon as the boron-carbide part appeared in the slices.

Since the goal was also to establish the presence of helium bubbles within the absorber, and better results could be expected when 256 intensity levels were applied during the reconstructions with the smoothing penalty term turned on, 100 cross-sections (from 2451 to 2550) of size 611×611 were reconstructed from 6 and 9 projections. The most convincing evidence of helium bubbles could be observed in the spatial visualization in Figure 10(b), where a large cavity was present via multiple slices.
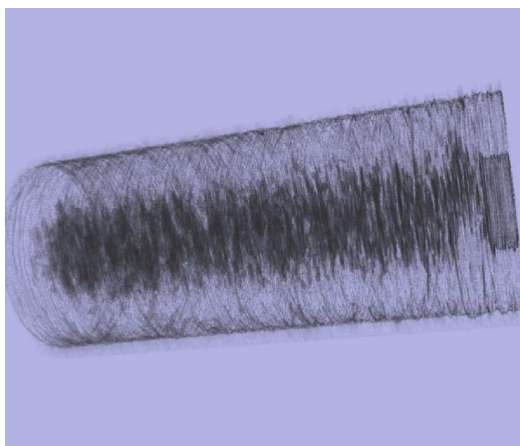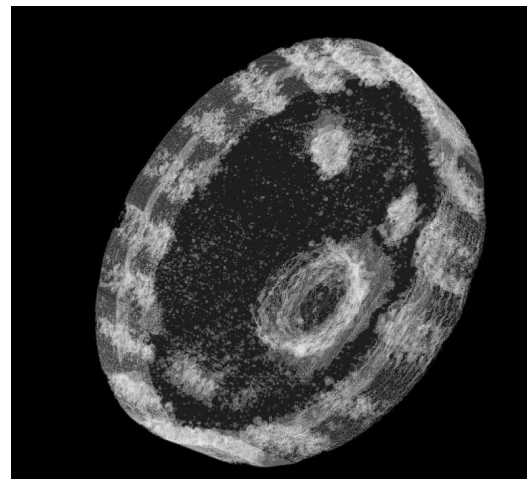
(a)   (b)

Figure 10: (a) Volume-rendered 3-dimensional visualization of the control rod with a transparent wall using three estimated intensity levels. (b) Volume-rendered view of 100 cross-sections using 256 intensity levels. The slices for both models were reconstructed by performing the pixel-based technique using 9 corrupted projections.

7 Conclusions

A new pixel-based DT technique was developed that is suitable for reconstructing objects comprising a small number of homogeneous materials from a few projections. The author verified the capabilities of the technique on software as well as physical phantoms, and also tested it using real physical measurements. Overall, it can be said that the pixel-based DT method can produce acceptable reconstruction results, even when the classical ones fail when there is a small number of projections. Under such circumstances, the DT technique reflects the real absorption values more properly than FBP and ART do, because it cannot show false intensity levels. This fact means that the pixel-based technique is especially suited for 3-dimensional visualizations, when ART and FBP do not perform well.

Key points of the dissertation

The reconstruction method and simulations

The results were published in [9, 10] and in a book chapter [5].

I/1. The author devised and developed a new pixel-based DT reconstruction technique that is suitable for reconstructing discrete images containing a few intensity levels from a limited number of parallel projections. In order to evaluate the technique on simulated data, he also implemented a parallel beam projection system to generate tomographic projections for arbitrary grey-level images. [5, 9] (sections 2.3 and 3.1)

I/2. The author analyzed the input parameters, and determined a possible set-up of initial reconstruction arguments. In a simulation environment, the author tested the pixel-based reconstruction technique to see how it performed when its parameters were changed within some reasonable range. The subjects of the investigation were the number of projections used for a reconstruction, the initial temperature, the cooling factor, the termination criterion, the variance needed to determine the equilibrium state, and the amount of noise added to the projections. In addition, he also tested whether the method displayed any sensitivity to the geometrical structure of the object to be reconstructed. [5, 9] (sections 3.2.3 and 3.3)

I/3. For the simulation of the greatest distorting effect of real measurements, the author developed a noise generator, which was designed to corrupt the perfect projections by additive Gaussian noise. Since the results reflected a strong sensitivity to statistical noise, he proposed, developed, and tested a smoothness prior as a regularization term in the objective functional. [10] (Section 3.4)

I/4. The author constructed two possible extensions to enable the technique to reconstruct multi-level discrete images, and tested the extension on 3-level phantoms under ideal noiseless as well as noisy conditions. [10] (Section 3.5)

Pre-processing

The results were published in [1, 12].

II/1. As the tomographic projections are usually corrupted by a number of different effects, the author devised a possible sequence of pre-processing steps for the common distortions encountered in the physical measurements. He also introduced two new pre-processing steps, namely intensity and motion corrections. [12] (Section 4.5)

II/2. The author examined the benefits of utilizing the pre-processing steps on the classical FBP reconstructions of VIDICON tube cross-sections. [1, 12] (Section 4.6)

Applications

The results were published in [3, 9, 10, 12, 13] and in a book chapter [5].

III/1. The author provided and applied a technique that is capable of determining the approximate values of the intensity levels, which are usually unknown in the case of physical examinations. [5] (Section 5.1.2)

III/2. The author performed the pre-processing steps and reconstructed the X-ray, neutron and gamma-ray projections of a Plexiglas, an iron, and an aluminum reference cylinder, respectively. In order to compare the pixel-based method with the classical ones, FBP and ART reconstructions were also constructed using the SNARK93 programming system. [10, 12] (Chapter 5)

III/3. Within the cooperation of the Hahn-Meitner Institute (Berlin), the author reconstructed a cardiac pacemaker battery from a limited number of X-ray projections, where the homogeneity of the materials could not be assumed. Based on the reconstructed cross-sections, the author constructed a spatial model, which clearly revealed the presumed irregular distribution of the electrically charged intrinsic material. [9] (Section 6.1)

III/4. The author performed reconstructions from a small number of neutron projections of a boron-carbide control rod provided by the Hungarian Academy of Sciences KFKI Atomic Energy Research Institute (Budapest). He also constructed a 3-dimensional visualization of the reconstructed cross-sections and confirmed the irregular absorber distribution as well as the helium accumulations in the lower section of the rod. [3] (Section 6.2)

III/5. The author participated in the development of the `DIRECT` system, integrated the reconstruction method with the `DIRECT` framework, and published the pixel-based technique via the `DIRECT` Web interface. [13] (Chapter 7)

References

[1] M. Balaskó, A. Kuba, A. Nagy, Z. Kiss, L. Rodek, and L. Ruskó. Neutron-, gamma- and X-ray three-dimensional computed tomography at the Budapest research reactor site. *Nuclear Instruments and Methods in Physics Research A*, 542:22–27, 2005.

[2] M. Balaskó, A. Kuba, A. Tanács, Z. Kiss, A. Nagy, and B. Schillinger. Comparison Radiography and Tomography Possibilities of FRM-II (20 MW) and Budapest (10 MW) Research Reactor. In *Proceedings of the Eighth World Conference WCNR-8*, pages 18–27, 2008.

[3] M. Balaskó, E. Sváb, Z. Kiss, A. Tanács, A. Nagy, and A. Kuba. Study of the inner structure of a damaged control rod by neutron and X-ray radiography and discrete tomography. In *Proceedings of the Eighth World Conference WCNR-8*, pages 294–303, 2008.

[4] M. Balaskó, E. Sváb, A. Kuba, Z. Kiss, L. Rodek, and A. Nagy. Pipe corrosion and deposit study using neutron- and gamma- radiation sources. *Nuclear Instruments and Methods in Physics Research A*, 542:302–308, 2005.

[5] J. Baumann, Z. Kiss, S. Krimmel, A. Kuba, A. Nagy, L. Rodek, B. Schillinger, and S. Juergen. *Discrete tomography methods for non-destructive testing in [8]*, pages 303–332. Birkhäuser, Boston, 2007.

[6] M. T. Chan, G. T. Herman, and E. Levitan. *Probabilistic Modeling of Discrete Images in [7]*, pages 213–235. Birkhäuser, Boston, 1999.

[7] G. T. Herman and A. Kuba, editors. *Discrete Tomography. Foundations, Algorithms, and Applications*. Birkhäuser, Boston, 1999.

[8] G. T. Herman and A. Kuba, editors. *Advances in discrete tomography and its applications*. Birkhäuser, Boston, 2007.

[9] Z. Kiss, L. Rodek, and A. Kuba. Image reconstruction and correction methods in neutron and X-ray tomography. *Acta Cybernetica*, 17:557–587, 2006.

[10] Z. Kiss, L. Rodek, A. Nagy, A. Kuba, and M. Balaskó. Reconstruction of pixel-based and geometric objects by discrete tomography. Simulation and physical experiments. *Electronic Notes in Discrete Mathematics*, 20:475–491, 2005.

[11] S. Krimmel, J. Baumann, Z. Kiss, A. Kuba, A. Nagy, and J. Stephan. Discrete tomography for reconstruction from limited view angles in non-destructive testing. *Electronic Notes in Discrete Mathematics*, 20:455–474, 2005.

[12] A. Kuba, L. Rodek, Z. Kiss, L. Ruskó, A. Nagy, and M. Balaskó. Discrete tomography in neutron radiography. *Nuclear Instruments and Methods in Physics Research A*, 542:376–382, 2005.

[13] A. Kuba, L. Ruskó, Z. Kiss, and A. Nagy. Discrete reconstruction techniques. *Electronic Notes in Discrete Mathematics*, 20:385–398, 2005.

[14] A. Kuba, L. Ruskó, L. Rodek, and Z. Kiss. Application of Discrete Tomography in Neutron Imaging. In *Proceedings of the Seventh World Conference WCNR-7*, pages 361–371, 2002.

[15] A. Kuba, L. Ruskó, L. Rodek, and Z. Kiss. Preliminary studies of discrete tomography in neutron imaging. *IEEE Trans. Nucl. Sci.*, 52:380–385, 2005.

[16] N. Robert, F. Peyrin, and M. J. Yaffe. Binary vascular reconstruction from a limited number of cone beam projections. *Medical Physics*, 21:1839–1851, 1994.

[17] A. Tanács and A. Kuba. Evaluation of a fully automatic medical image registration algorithm based on mutual information. *Acta Cybernetica*, 16:327–336, 2003.

The author's publications cited in the Thesis

Chapters in books

J. Baumann, Z. Kiss, S. Krimmel, A. Kuba, A. Nagy, L. Rodek, B. Schillinger, and S. Juergen. *Discrete tomography methods for non-destructive testing in [8]*, pages 303–332. Birkhäuser, Boston, 2007.

Articles in peer reviewed journals

Z. Kiss, L. Rodek, and A. Kuba. Image reconstruction and correction methods in neutron and X-ray tomography. *Acta Cybernetica*, 17:557–587, 2006.

Z. Kiss, L. Rodek, A. Nagy, A. Kuba, and M. Balaskó. Reconstruction of pixel-based and geometric objects by discrete tomography. Simulation and physical experiments. *Electronic Notes in Discrete Mathematics*, 20:475–491, 2005.

A. Kuba, L. Ruskó, Z. Kiss, and A. Nagy. Discrete reconstruction techniques. *Electronic Notes in Discrete Mathematics*, 20:385–398, 2005.

Full papers in conference proceedings

M. Balaskó, A. Kuba, A. Nagy, Z. Kiss, L. Rodek, and L. Ruskó. Neutron-, gamma- and X-ray three-dimensional computed tomography at the Budapest research reactor site. *Nuclear Instruments and Methods in Physics Research A*, 542:22–27, 2005.

A. Kuba, L. Rodek, Z. Kiss, L. Ruskó, A. Nagy, and M. Balaskó. Discrete tomography in neutron radiography. *Nuclear Instruments and Methods in Physics Research A*, 542:376–382, 2005.

M. Balaskó, E. Sváb, Z. Kiss, A. Tanács, A. Nagy, and A. Kuba. Study of the inner structure of a damaged control rod by neutron and X-ray radiography and discrete tomography. In *Proceedings of the Eighth World Conference WCNR-8*, pages 294–303, 2008.

Selected publications not included in the thesis

S. Krimmel, J. Baumann, Z. Kiss, A. Kuba, A. Nagy, and J. Stephan. Discrete tomography for reconstruction from limited view angles in non-destructive testing. *Electronic Notes in Discrete Mathematics*, 20:455–474, 2005.

A. Kuba, L. Ruskó, L. Rodek, and Z. Kiss. Preliminary studies of discrete tomography in neutron imaging. *IEEE Trans. Nucl. Sci.*, 52:380–385, 2005.

[3]M. Balaskó, E. Sváb, A. Kuba, Z. Kiss, L. Rodek, and A. Nagy. Pipe corrosion and deposit study using neutron- and gamma- radiation sources. *Nuclear Instruments and Methods in Physics Research A*, 542:302–308, 2005.

---

[3]Science Citation Index, Impact factor: 1.166

A. Kuba, L. Ruskó, L. Rodek, and Z. Kiss. Application of Discrete Tomography in Neutron Imaging. In *Proceedings of the Seventh World Conference WCNR-7*, pages 361–371, 2002.

M. Balaskó, A. Kuba, A. Tanács, Z. Kiss, A. Nagy, and B. Schillinger. Comparison Radiography and Tomography Possibilities of FRM-II (20 MW) and Budapest (10 MW) Research Reactor. In *Proceedings of the Eighth World Conference WCNR-8*, pages 18–27, 2008.